Bulletin of Earth Sciences of Thailand

Shale pore network and seepage simulation of Huai Hin Lat Formation

Soraya Suninbun[1*], Thitiphan Assawincharoenkij[2], Phakkhananan Pakawanit[3]

[1]Department of Geology, Faculty of Science, Chulalongkorn University, Bangkok, 10330 Thailand
[2]Applied Mineral and Petrology Research Unit (AMP RU), Department of Geology, Faculty of Science, Chulalongkorn University, Bangkok, 10330 Thailand
[3]Synchrotron Light Research Institute (Public Organization), 111 University Avenue, Muang district, Nakhon Ratchasima 30000, Thailand
[*] Correspondence author e-mail: Soraya.Suninbun@gmail.com

Received: 25 Apr 2025
Revised: 19 Jun 2025
Accepted: 20 Jun 2025

ABSTRACT

Gas shale is a type of unconventional petroleum reservoir characterized by low permeability, requiring stimulation techniques such as hydraulic fracturing to enable fluid flow and hydrocarbon extraction. It is associated with physical properties that complicate fluid migration pathways, posting challenges for the development of petroleum extraction and recovery in low-permeability shale formations. Furthermore, shale acts as an effective seal for carbon capture and storage (CCS) due to its low permeability and porosity. However, its complex pore structure, dominated by micropores, presents challenges in accurately measuring connected porosity. This study aims to investigate the pore morphology, pore network characteristics, and rock simulations of gas shale from the Dat Fa Member of the Huai Hin Lat Formation. Geochemical compositions were analyzed using XRD and XRF techniques to identify the rock type. Scanning electron microscopy (SEM) was used to examine 2D pore morphology, distribution, and total porosity. X-ray tomographic microscopy was used to generate pore network models, which were then used to calculate total and effective porosity for seepage flow simulations, enhancing the analysis of gas transport mechanisms in rock formations. Geochemical analysis classified the rock types as calcareous shale and dolomitic shale. SEM images of calcareous shale typically reveal parallel flat pores and pinch-outs along the laminations. Dolomitic shale exhibits laminations of dolomite and calcite, with micropores surrounding mineral grains. The total porosity values for calcareous shale and dolomitic shale are 5.54% and 3.04%, respectively. Micro-CT image analysis shows that the total porosity of calcareous shale ranges from 2.86% to 4.65%, while the effective porosity decreases to between 0.83% and 1.75%. For dolomitic shale, total porosity ranges from 3.51% to 3.70%, and effective porosity ranges from 1.99% to 3.27%. Seepage simulations indicate that calcareous shale exhibits greater diffusivity along parallel laminations, whereas dolomitic shale demonstrates higher diffusivity across perpendicular laminations.

Keywords: porosity, pore morphology, pore network, rock simulation, XTM

1. Introduction

The global energy industry is transforming toward more sustainable alternatives, with carbon capture and storage (CCS) emerging as a key technology for reducing greenhouse gas emissions. Shale plays a crucial role in these systems, serving both as a hydrocarbon source rock and an effective seal for subsurface storage. A thorough understanding of shale's physical properties, particularly porosity and permeability, is essential for improving energy extraction processes and optimizing CCS operations (Askarova et al., 2023; Chenrai et al., 2022a; Saraf and Bera, 2021).

Shale is a fine-grained sedimentary rock characterized by a complex pore structure predominantly comprised of micropores. Due to its extremely low permeability, advanced analytical techniques such as micro-computed tomography (Micro-CT) and scanning electron microscopy (SEM) are required to examine micropore characteristics (Bollermann et al., 2022). Three-dimensional (3D) models generated from micro-CT scans offer critical insights into pore distribution and connectivity, facilitating quantitative analysis of porosity and permeability (Song et al., 2021). Pore network models further enable the simulation of fluid flow dynamics in shale, providing valuable understanding on seepage behavior and migration pathways at microscale (Jing et al., 2021).

Recent advances in shale porosity analysis using SEM have enabled high-resolution imaging of pore shape, total porosity, and pore distribution. In addition, micro-CT imaging has emerged as a vital tool for developing 3D pore network models, supporting the estimation of total and effective porosity as well as the simulation of fluid dynamics through interconnected pores (Bollermann et al., 2022; Cid et al., 2017; Jing et al., 2021; Khan et al., 2022; Lin et al., 2020; Song et al., 2021; Zhang et al., 2018). Despite these advancements, significant gaps remain in understanding how pore network connectivity and lamination orientation influence fluid transport in microporous shales. Advanced modeling techniques, including isotopic pore distribution analysis, enhance the characterization of pore size and throat radius, and facilitate the evaluation of fluid migration dynamics, particularly in relation to flow parallel or perpendicular to laminations (Bollermann et al., 2022; Jing et al., 2021).

This study aims to address these understanding gaps through studying shale micropore morphology, pore networks, and fluid flow simulations. This research examines the implications of effective porosity and lamination orientation on fluid migration in shale formations (Javadpour et al., 2007; Jing et al., 2021). The results will enhance the understanding of shale's capacity for significant hydrocarbon storage and movement, in addition to its role as a caprock in carbon capture and storage applications. A thorough investigation of pore morphology and seepage dynamics is crucial for enhancing unconventional resource extraction methods and optimizing carbon storage strategies. This research provides important insights for future developments in energy extraction and environmental mitigation technologies, considering the increasing role of shale in energy development and carbon capture and storage (Arsairai et al., 2016a; Chenrai et al., 2022a; Han et al., 2020; Javadpour et al., 2007).

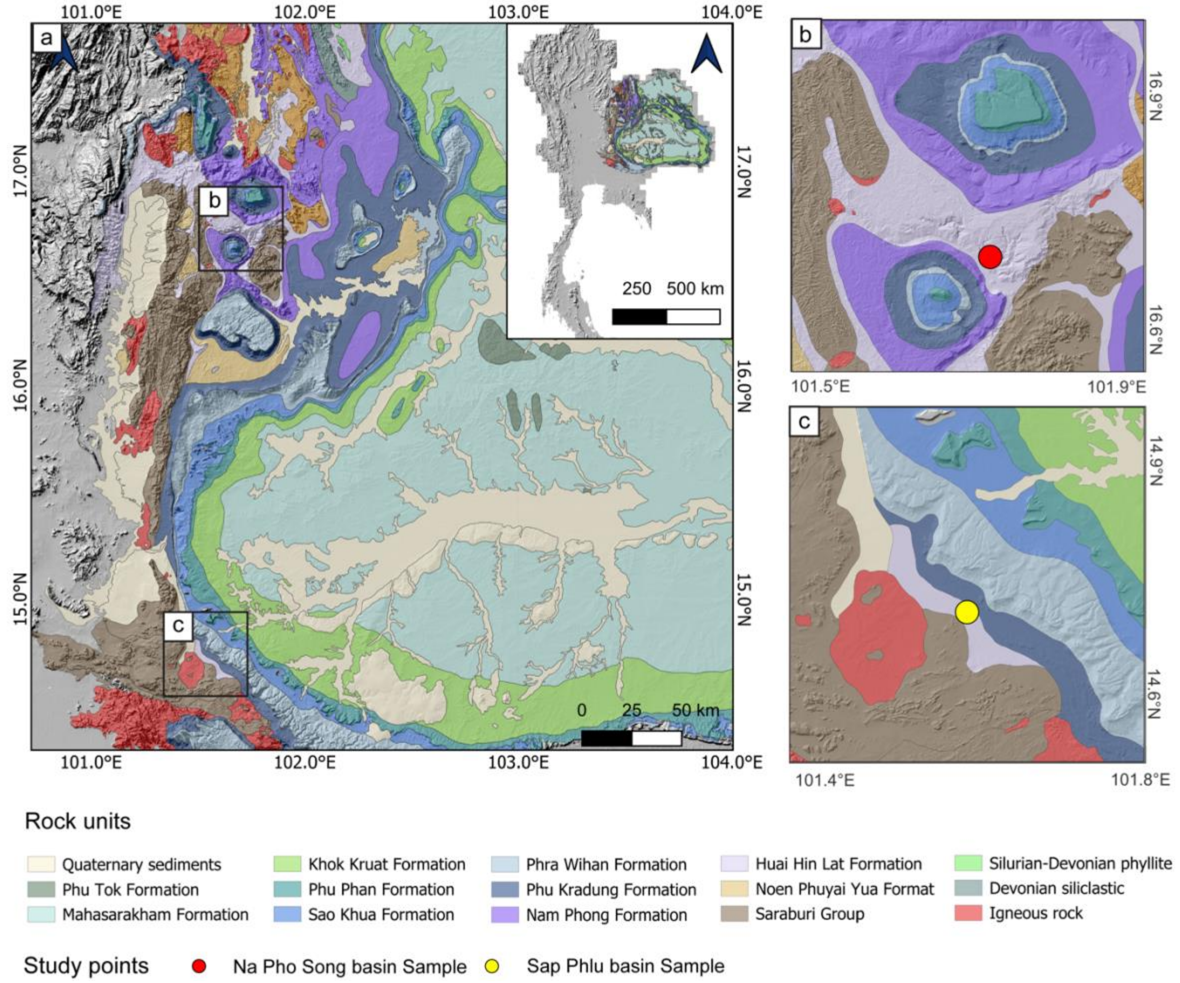

Figure 1. The geological map shows (a) the distribution of rock units in northeastern Thailand, focusing on the Huai Hin Lat Formation's expanded exposure; (b) the samples collected in the Na Pho Song Basin, Phetchabun Province; and (c) the samples in the Sap Phlu Basin, Nakhon Ratchasima Province (modified from DMR (2013)).

2. Geological setting

The Huai Hin Lat Formation, located beneath the Khorat Group, plays an essential role in determining the geological development of northeastern Thailand (Arsairai et al., 2016b). This formation is predominantly composed of dark-gray mudstone, sandstone, and conglomerate, which were deposited in a fluvio-lacustrine environment during the Triassic period (Chenrai et al., 2022a). It has been classified into five lithostratigraphic members: I Mo, Phu Hi, Dat Fa, Sam Khean, and Pho Hai. The Dat Fa Member is notably significant, composed of gray to black calcareous shale and argillaceous limestone (Chitnarin et al., 2022).

The organic material in the Dat Fa Member predominantly originates from terrestrial plant debris, with minor contributions from algae. This composition conforms to kerogen type III, associated with gas-prone source rocks (Chenrai et al., 2022a; Chitnarin et al., 2022). The depositional conditions, together with the preservation of organic materials, indicate that the Dat Fa Member may be an important source of shale gas in the region (Chenrai et al., 2022a).

Shale samples were collected from the Na Pho Song and and Sap Phlu basins (Figure 1), which are both categorised as Late Triassic half-graben basins within the Khorat Plateau (Chonglakmani and Sattayarak, 1978; Lovatt Smith et al., 1996). Although the Huai Hin Lat Formation's organic-rich shales are found in both basins, their sizes and depositional environments are different. Dolomitic shale, which may have been created under more constrained or evaporitic lacustrine conditions, is found in the wider Na Pho Song Basin. Conversely, calcareous shale, which indicates more lacustriner depositional settings, is found in the smaller Sap Phlu Basin (Arsairai et al., 2023; Khositchaisri, 2012).

3. Material and methods

In this study, shale samples from the Na Pho Song Basin (dolomitic shale) and Sap Phlu Basin (calcareous shale), part of the Dat Fa Member, were analyzed to assess the rock porosity of the gas shale.

3.1 Mineral and Geochemical Analyses

Shale samples from the Na Pho Song and Sap Phlu Basins, which included calcareous shale and dolomitic shale, were selected for analysis. A systematic sample preparation procedure was implemented to ensure high-quality and consistent samples for geochemical analysis. The initial step involved cleaning the samples with ethanol to remove surface impurities, followed by desiccation at 60°C for 6 h to eliminate any residual moisture. Subsequently, the samples were crushed using a jaw crusher and homogenized using the coning and quartering techniques to ensure uniformity. The resulting material was finely ground into a powder using a disc mill, rendering it suitable for advanced analysis, including X-ray diffraction (XRD) and X-ray fluorescence (XRF).

The XRD analysis was conducted using a Bruker AXS D8 Advance X-ray diffractometer at the Department of Geology, Chulalongkorn University, Bangkok, with a copper target emitting radiation of 1.5406 Å, operating at 40 kV and 30 mA. The systematic scan range was from 5° to 80° 2θ, with a step size of 0.02° and a counting duration of 1 s per step.

XRF analysis, utilizing a Bruker AXS S4 pioneer wavelength-dispersive X-ray fluorescence (WDXRF) spectrometer, enabled detailed elemental analysis. The instrument operated at 60 kV and 50 mA, with an energy range of 0.2-20 Å (60-0.6 keV) for precise elemental detection. Sample preparation involved combining 8 g of finely milled rock powder with 1 g of microwax, forming a pellet that was placed into the sample chamber of the spectrometer. Calibration was performed with certified reference materials, and elemental quantification was performed using the Bruker SPECTRA Plus software, allowing for accurate chemical composition analysis.

3.2 Scanning Electron Microscopy (SEM) Imaging

The preparation of polished thin sections for SEM involved several steps to ensure optimal surface quality for imaging. Samples were cleaned with ethanol, dried thoroughly, and sliced into slabs approximately 2 x 3 x 0.1 cm. The slabs were polished to a mirror-like finish, essential for high-resolution imaging, and then heated to ensure dryness before being mounted on glass slides with epoxy resin. A thin layer of carbon was applied to the samples to reduce charging effects during imaging.

SEM imaging was performed using an electron probe microanalyzer (EPMA; JEOL JXA-iSP100 model, Japan) at the Department of Geology, Faculty of Science, Chulalongkorn University, which uses a focused electron beam to produce high-resolution images of the sample surfaces. The SEM analysis was conducted under high vacuum conditions at a landing voltage of 20 kV. A backscattered electron detector (BSED) was used for capturing images at magnifications of 50x to 3,000x, revealing detailed surface morphology and microstructural features. Energy dispersive X-ray spectroscopy (EDS) was utilized for elemental analysis, providing compositional data that were processed with Fiji (ImageJ) software to measure particle size and morphology. These SEM results were critical for understanding the complex pore structures, particularly the interconnected micropores that are essential for petroleum migration and storage.

3.3 Micro-CT Scan Imaging

Rock sample preparation for X-ray tomographic microscopy (XTM) (scintillator-coupled X-ray microscopes) involved cleaning with ethanol and drying to remove contaminants. The samples were then placed in an oven at 60°C for 6 hours to eliminate moisture. Samples were carefully prepared with a diameter of 0.5 mm and a height of 1 mm and classified based on lamination orientation into sample names: calcareous shale-v, calcareous shale-h, dolomitic shale-v, and dolomitic shale-h. This classification enabled a detailed investigation of vertical (v) and horizontal (h) lamination features.

XTM was used to generate 3D images of the internal rock structure through X-ray attenuation. High-energy X-rays were directed through the samples, producing two-dimensional (2D) radiographic images. These images were processed with denoising, filtering, and binarization techniques, which enabled the reconstruction of 3D models. This method is particularly effective for evaluating porosity at sub-micrometer resolutions, revealing pore size distribution and material density differentiation. The scans were conducted at Beamline 1.2W of the Synchrotron Light Research Institute (SLRI), Nakhon Ratchasima, Thailand, using specifications provided in Table 1.

Table 1 Specifications of the X-ray Tomographic Microscopy (XTM) system at Beamline 1.2W of the Synchrotron Light Research Institute (SLRI), Nakhon Ratchasima, Thailand.

Source	Multi-pole wiggler, 2.2T
Radiation type	Polychromatic beam
Energy range	5-20 keV
Imaging efficiency	100 frames/s
Beam size	10 x 4 mm (H x V)
Spatial resolution	1.5 µm (pixel size 0.72 µm)
Projection	Optique Peter, WB microscope 5X, 10X
Data acquisition/Analysis	LABView-based: XIMaq, XIMove, Octopus
Detector	YAG-Ce scintillation, sCMOS camera (PCO.edge 5.5)

3.4 3D Models and Rock Simulation

The pore network of each rock layer was reconstructed using micro-CT scan images and segmented using Dragonfly software (Meng et al., 2024). This segmentation enabled the calculation of pore and rock volumes based on grayscale intensity values, which were then compared with SEM-derived porosity estimates.

Segmentation of the micro-CT images was performed to identify pore spaces, with the lowest grayscale values representing voids and the highest indicating mineral grains. This binary segmentation process allowed the development of 3D models, which were used to create a pore network model (PNM). The model was generated by selecting regions of interest (ROIs) that included both the solid mineral grains and the pore spaces, facilitating the accurate calculation of total porosity.

The PNM was refined by applying specific parameters, such as phase index, sigma, and Rmax, to maintain the integrity of small pores and preserve the largest pore features. The analysis of pore size distribution revealed a range of pore sizes, with the relationship between pore throat size and distance providing insights into fluid transport characteristics. The PNM was subsequently used for fluid seepage simulation under air conditions, providing valuable data on effective porosity and permeability. The seepage simulation was conducted using the Navier-Stokes and Darcy's Law models to simulate fluid movement through the rock, with the results showing varying diffusivity depending on lamination orientation.

In summary, the combination of XRD, XRF, SEM, micro-CT scan, and 3D pore network modeling provided a comprehensive methodology for analyzing the geochemical composition, pore structure, and fluid dynamics within the rock samples from the Huai Hin Lat Formation. These results contribute to a more profound understanding of the potential for shale gas exploration in this formation.

4. Results and discussions

4.1 Mineral and Chemical Characteristics

Mineral compositions of shale samples from the Na Pho Song and Sap Phlu Basins are shown in Table 2. The investigation provides essential insights into the geological classifications and formation processes of these rocks. The results indicate that carbonate minerals predominate in the samples. The calcareous shale from the Sap Phlu Basin is predominantly made of calcite and quartz, with some clay minerals, whereas the dolomitic shale from the Na Pho Song Basin primarily contains dolomite, calcite, quartz, and albite.

Table 2 The percentage of each mineral observed in the samples, providing a comparative analysis of the mineral content.

Sample no.	Calcareous shale	Dolomitic shale
Calcite	88.57	24.91
Quartz	10.57	11.15
Dolomite	-	52.41
Albite	-	11.53
Talc	0.82	-

The elemental composition of the rock samples was measured by X-ray fluorescence (XRF) spectroscopy, resulting in an extensive analysis of the major oxides in the rock matrix

(Table 3). The results indicate that calcareous shale predominantly consists of CaO (78.55 wt.%). Dolomitic shale presents a significant dolomitic composition, with MgO (7.12 wt.%) and CaO (29.40 wt.%), which corresponds with the mineralogical formula $CaMg(CO_3)_2$.

Table 3 The primary composition of the analyzed calcareous shale and dolomitic shale samples in weight percent (wt.%).

Sample no.	Calcareous shale	Dolomitic shale
Al_2O_3	2.23	13.07
CaO	78.55	29.4
Fe_2O_3	1.69	6.8
K_2O	0.25	3.74
MgO	1.22	7.12
MnO	0.19	0.12
P_2O_5	0.38	0.1
SiO_2	15.08	38.28
SO_3	0.07	0.54
SrO	0.27	0.24

Understanding these chemical variations is crucial for identifying carbonate rocks and analyzing their depositional environments. The high content of CaO in calcareous shale and MgO in dolomitic shale suggests these fine-grained, carbonate-rich, argillaceous minerals were deposited in organic-rich environments. These conditions enhance their capacity as hydrocarbon source rocks or caprock seals for petroleum systems (Bollermann et al., 2022; Chenrai et al., 2022a; Dyni, 2004).

4.2 Pore morphology

Scanning electron microscopy (SEM) imaging revealed significant variations in pore morphology of carbonate shale between calcareous shale and dolomitic shale. The morphology of shale samples showed perpendicular interconnected flat pores, whereas the calcareous shale exhibited significant petrological characteristics, such as flat pores, lamination, and pinch-out structures along parallel laminations (Figure 2a). The pores, identified as dark areas in the SEM images, correspond to regions of mineral dissolution, forming connected pore spaces. Flat porosity was predominantly related to parallel laminations and individual pores terminating within separate layers, revealing a varied composition of carbonate and silicate minerals (Figure 2b).

SEM imaging showed high-porosity layers within the calcareous shale, consisting of dense mineral grains and flat pores (Figure 2c), which considerably influenced porosity and permeability. Image analysis using Fiji-ImageJ software estimated the total porosity of the calcareous shale to be approximately 5.54%, with interconnected porosity zones accounting for 15.56% (Figure 2d). Energy-dispersive X-ray spectroscopy (EDS) examination verified the elemental composition of various mineral phases, indicating that the lighter grey minerals at Spot 1 were rich in calcium (Figure 2e), whereas the darker grey minerals at Spot 2 were rich in silicon (Figure 2f).

The porosity distribution in calcareous shale demonstrated considerable anisotropy, with a greater abundance of pores along parallel laminations than in perpendicular laminations. Moreover, quartz-rich zones showed reduced porosity compared to carbonate-rich areas, affecting gas transport dynamics. Mineral dissolution significantly contributed to the development of intergranular and interconnected pore spaces, which enabled fluid movement (Rashid et al., 2015). Calcite readily dissolves when in contact with fluids, and this dissolution process generates pore spaces within the rock. These pores often form in a parallel orientation, that functioned as channels for fluid flow (MacInnis and Brantley, 1992).

SEM imaging of dolomitic shale revealed interfingering laminated mineral layers (Figure 3a), characterized by the heterogeneous deposition of magnesium-rich (dark grey) and calcium-rich (light grey) minerals. The observed porosity (black) developed between mineral grains (Figure 3b). Flat porosity was primarily observed in magnesium-rich (dolomite) minerals, mixed with calcium-rich (calcite) minerals, where the grains showed perpendicular laminations (Figure 3c). The dolomite-rich zone (Figure 3d) displayed a flat pore shape along parallel laminations. Image analysis using Fiji-ImageJ software evaluated total porosity (blue) at 3.04%, indicating that fluid transport attributes were impacted by the extent of the pore network. EDS analysis indicated that the lighter grey minerals at Spot 1 were enriched in calcium (Figure 3e), while the grey minerals at Spot 2 were rich in both calcium and magnesium (Figure 3f).

SEM-based pore characterization provides significant insight into porosity evolution, improving the understanding of the mechanical characteristics and fluid transport behaviors of carbonate rock formations (Zhou et al., 2016). The transport of gas in these rocks is mainly controlled by micropore structures (Arsairai et al., 2016a). In calcareous shale and dolomitic shale, macro-intergranular flat pores are connected by smaller throat pores, mainly oriented along perpendicular laminations (He et al., 2014). The related pores facilitated the migration of gas and fluid, mixing between light and dark mineral zones within the laminations, thus demonstrating an anisotropic pore distribution. Differences in mineral composition and phase distribution considerably affected pore network formation and total porosity (Khan et al., 2022).

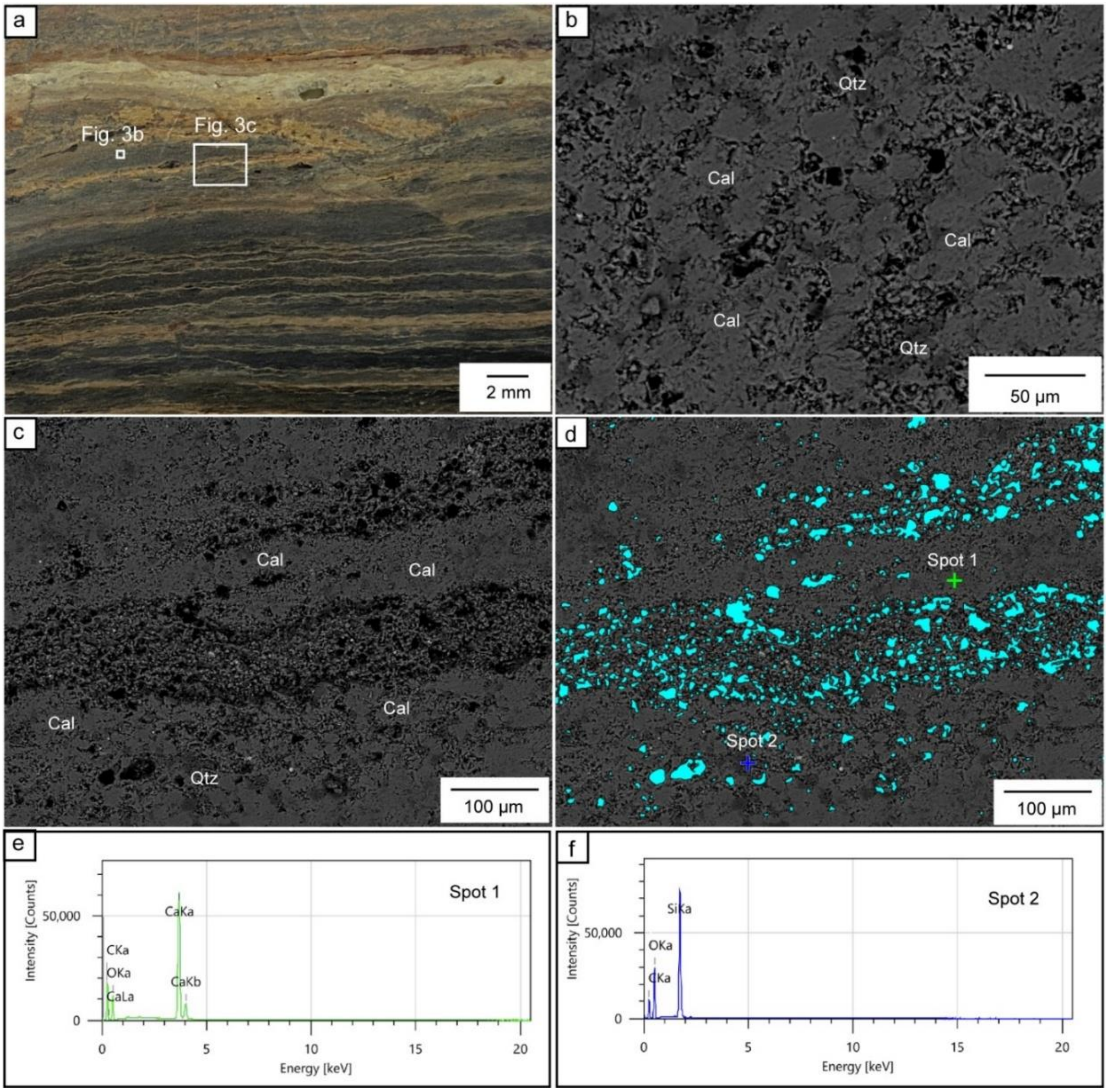

Figure 2. (a) Thin section showing the laminated structure, presented with scanning electron microscopy (SEM) images of calcareous shale, highlighting primary minerals including calcite (Cal) and quartz (Qtz): (b) Porosity within dense calcite; (c) Pinch-out feature between porosity and calcite lamination; (d) Porous layer with prominent pores as determined using by Fiji-ImageJ software; (e) EDS spectrum of calcium-rich mineral grain at Spot 1; and (f) EDS spectrum of silica-rich mineral grain at Spot 2.

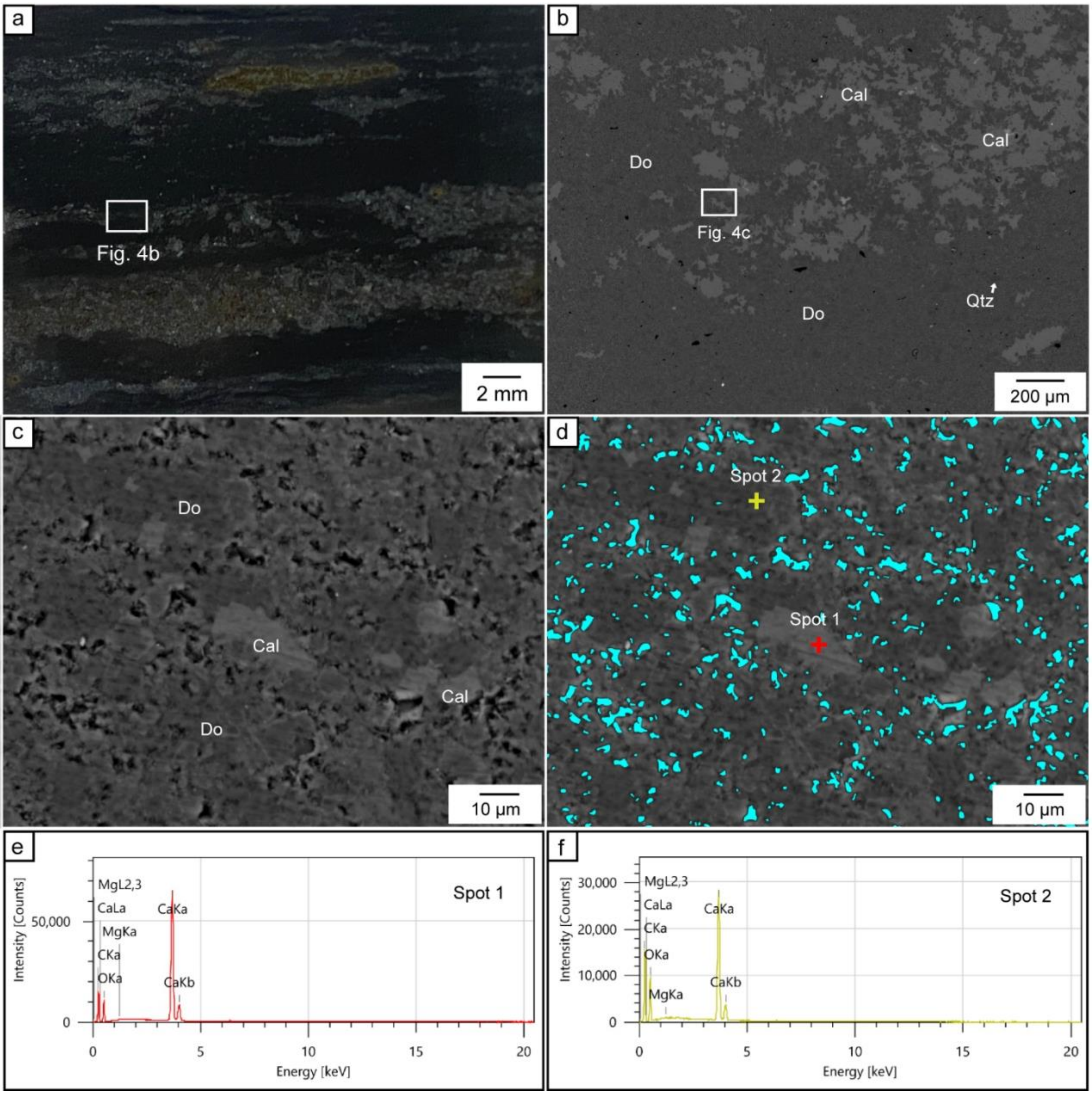

Figure 3. (a) Thin section showing the lamination structure, with SEM images of dolomitic shale highlighting primary minerals such as dolomite (Do), calcite (Cal), and quartz (Qtz); (b) pinch-out structure between dolomite and calcite laminations; (c) interconnected porosity around crystal grains; (d) porous layer with evident pores as indicated by Fiji-ImageJ software. (e) EDS spectrum of calcium-rich mineral grain at Spot 1, and (f) EDS spectrum of calcium- and magnesium-rich mineral grain at Spot 2

4.3 Rock Porosity and Pore Network

The 3D model of the pore network utilized millimeter-scale samples to achieve optimal resolution of perpendicular and parallel features in calcareous shale and dolomitic shale (Figures 4a, 5a, 6a, and 7a), using a Micro-CT pixel resolution of 0.72 µm. The selected area within the samples was analyzed to evaluate total porosity through grayscale segmentation of the Micro-CT data (Figures 4b, 5b, 6b, and 7b). The results gathered from SEM imaging by Fiji-ImageJ software indicated a strong correlation with Micro-CT scan data (Figures 2 and 3), revealing slight variations in porosity estimation.

Pore network models for calcareous shale were generated using Dragonfly software, with segmentation analyses performed on both perpendicular (calcareous shale-v) and parallel (calcareous shale-h) laminated orientations (Figures 4 and 5). Calcareous shale-v demonstrated concentrated dense porosity in a specific layer (Figure 4c), while calcareous shale-h showed pores distributed in parallel layers with various densities (Figure 5c). The results indicated that calcareous shale-h exhibited greater pore and throat diameters compared to calcareous shale-v, which directly impacted the total and effective porosities of each sample. The quantitative study indicated that calcareous shale-v had a total porosity of 2.86%, while calcareous shale-h demonstrated a greater porosity of roughly 4.65%. The samples were interconnected by throat channels ranging from 0.001 to 0.01 mm for both calcareous shale-v and calcareous shale-h (Figures 4d and 5d), with the resultant 3D models of pore networks displayed in Figures 4e and 5e.

Both calcareous shale samples showed a decrease in effective porosity compared to total porosity; however, calcareous shale-v had an effective porosity of 0.83%, while calcareous shale-h had a greater effective porosity of 1.75%. This evidence indicates that parallel laminations provided better pore connectivity and greater fluid transport channels in comparison to perpendicular laminated structures (Figures 4f and 5f).

Pore network models for dolomitic shale were generated using segmentation analyses performed in both perpendicular (dolomitic shale-v) and parallel (dolomitic shale-h) orientations (Figures 6 and 7). Dolomitic shale-v displayed a widespread distribution of pores across the rock layers, with zones of greater density and pinch-outs apparent in the parallel layers (Figure 6c). Dolomitic shale-h exhibited a comparable dense pore distribution in specific areas but demonstrated a more dispersed distribution along the parallel plane (Figure 7c). The results demonstrated that dolomitic shale-v exhibited greater pore and throat diameters compared to dolomitic shale-h. The quantitative analysis indicated that dolomitic shale-v demonstrated a total porosity of approximately 3.70%, while dolomitic shale-h revealed a slightly reduced total porosity of 3.51% (Figures 6d and 7d). The pores in both orientations were interconnected by throat channels ranging from 0.001 to 0.01 mm, as illustrated in the constructed 3D models of pore networks (Figures 6e and 7e).

Both dolomitic shale samples displayed a decline in effective porosity compared to total porosity, with dolomitic shale-v at 3.70% and dolomitic shale-h at 3.51%. This evidence indicates that perpendicular laminations provided higher pore connectivity and greater fluid transport channels in comparison to parallel laminated structures (Figures 6f and 7f).

This study revealed that effective porosity in gas shale tends to decrease as total porosity increases, following the trends observed in both perpendicular and parallel laminations. This decrease is closely related to the enhanced diffusivity in lamination-aligned pore distributions, which is crucial in forecasting fluid transport behavior in these formations (Cid et al., 2017). Sedimentary rocks typically have anisotropic pore distribution, which results in different pore connectivity both parallel and perpendicular to the laminations (Jing et al., 2021). The significance of these porosity trends is supported by seepage simulation results, suggesting that macropore fluid flow can be accurately modeled using advanced techniques such as fluid injection (Han et al., 2020). However, the parallel orientation in calcareous shale still exhibited more porosity than either dolomitic shale sample. These findings highlight the impact of mineralogical composition and fabric orientation on pore shape and connectivity, which are essential aspects in fluid migration and reservoir quality evaluations.

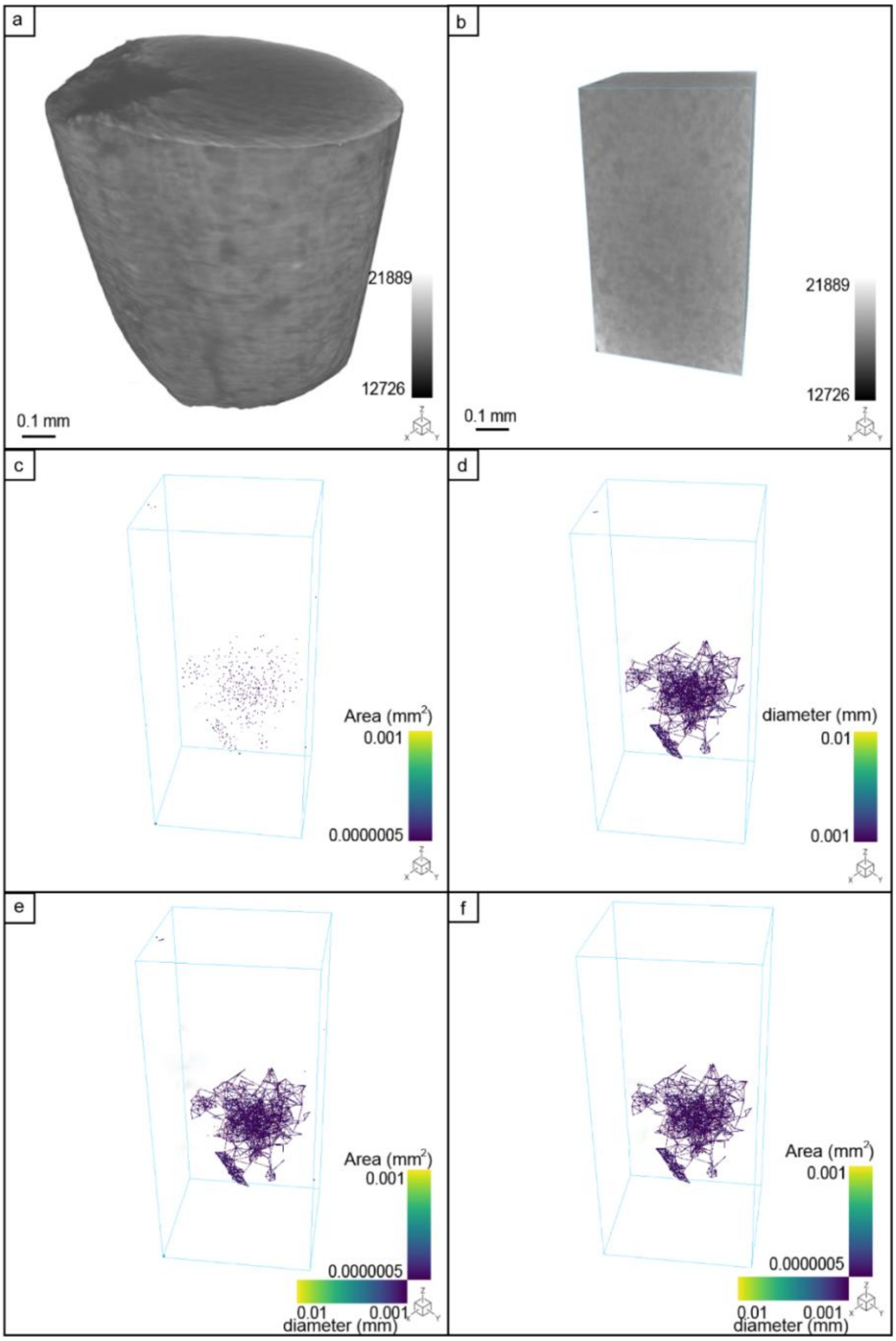

Figure 4. 3D Model analysis of the calcareous shale-v sample with Micro-CT images: (a) High-resolution image obtained with a 10x objective magnification and a pixel resolution of 0.72 µm; (b) Region of Interest (ROI) within the 3D model, measuring 0.54 x 0.67 x 0.97 mm³; (c) Distribution of pore diameters, ranging from 1.59 to 6.06 µm; (d) Throat diameters, varying from 0.001 to 0.01 mm; (e) Pore network connectivity indicating a porosity of 2.86%; and (f) Effective porosity, estimated at 0.83%.

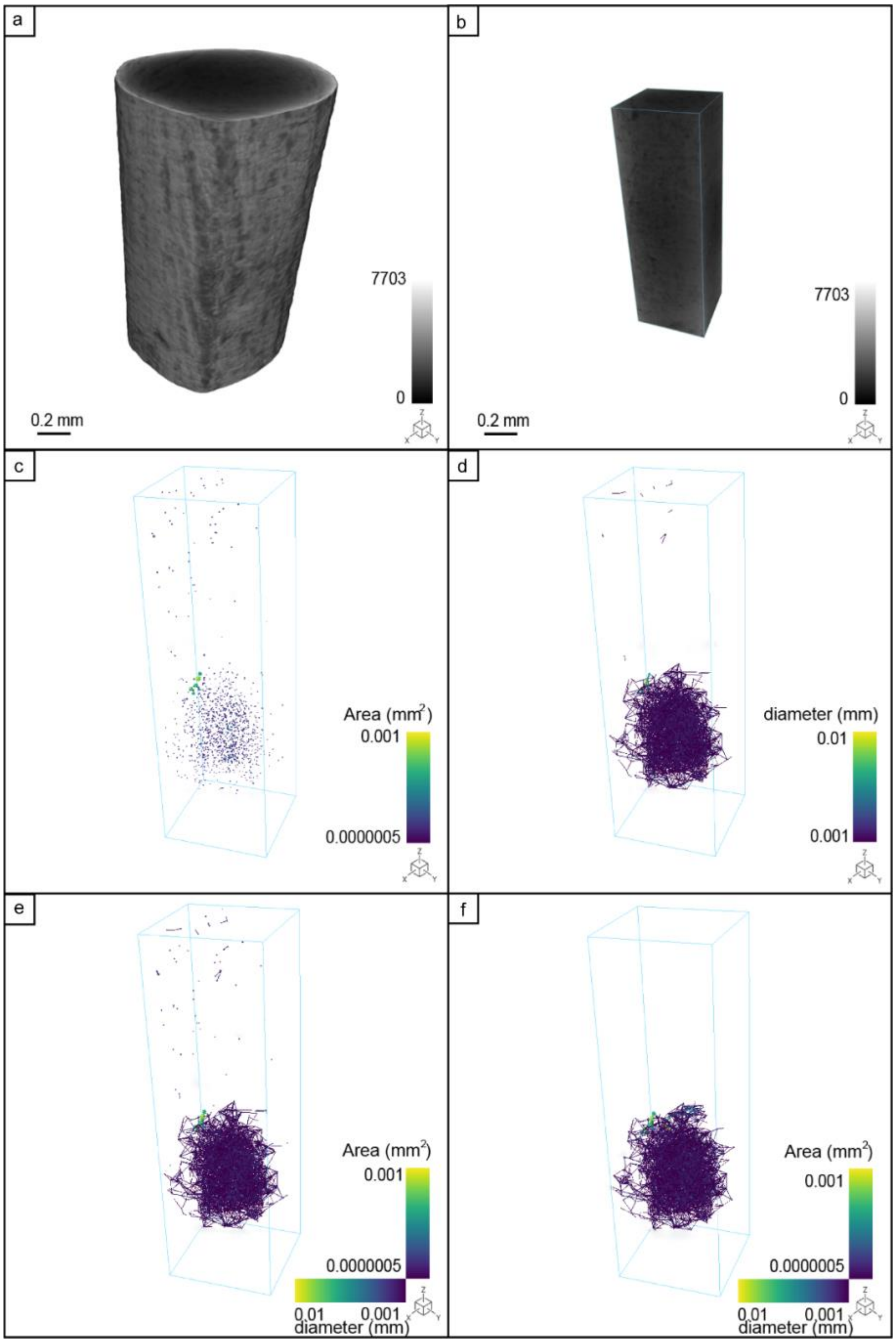

Figure 5. 3D Model analysis of the calcareous shale-h sample utilizing Micro-CT imaging: (a) High-resolution image obtained with a 10x objective magnification and a pixel resolution of 0.72 µm; (b) Region of Interest (ROI) within the 3D model, measuring 0.48 x 0.59 x 1.51 mm^3; (c) Distribution of pore diameters, ranging from 1.21 to 8.28 µm; (d) Throat diameters ranging from 0.001 to 0.01 mm; (e) Pore network connectivity indicating a porosity of 4.65%; and (f) Effective porosity, estimated at 1.75%.

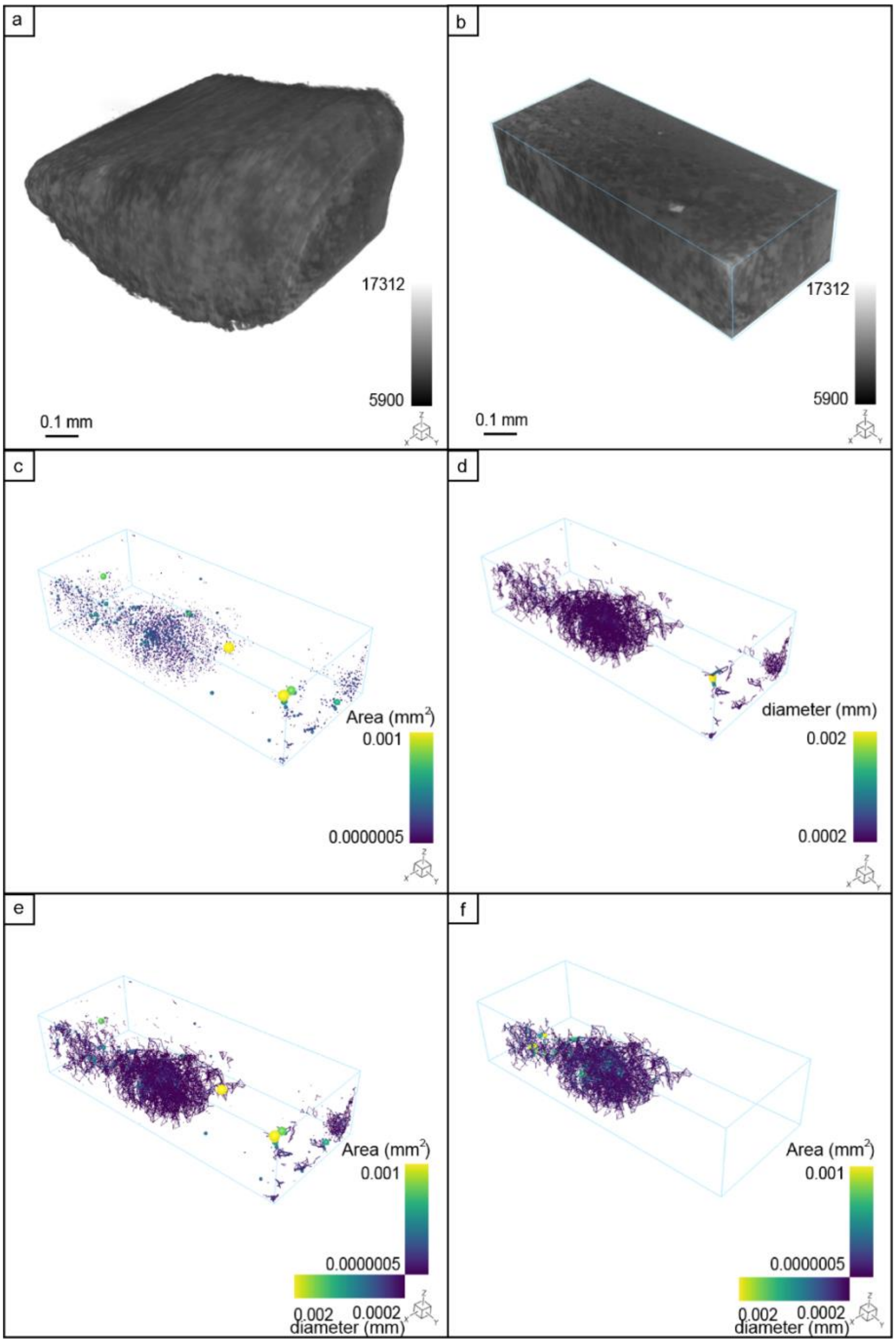

Figure 6. 3D Model analysis of the dolomitic shale-v sample conducted using Micro-CT images: (a) High-resolution image; (b) Region of Interest (ROI) within the 3D model, measuring 0.34 x 0.56 x 1.43 mm^3; (c) Distribution of pore diameters ranging from 0.77 to 10.75 µm; (d) Throat diameters ranging from 0.0002 and 0.002 mm; (e) Pore network connectivity indicating a porosity of 3.70%; and (f) Effective porosity, estimated at 3.27%.

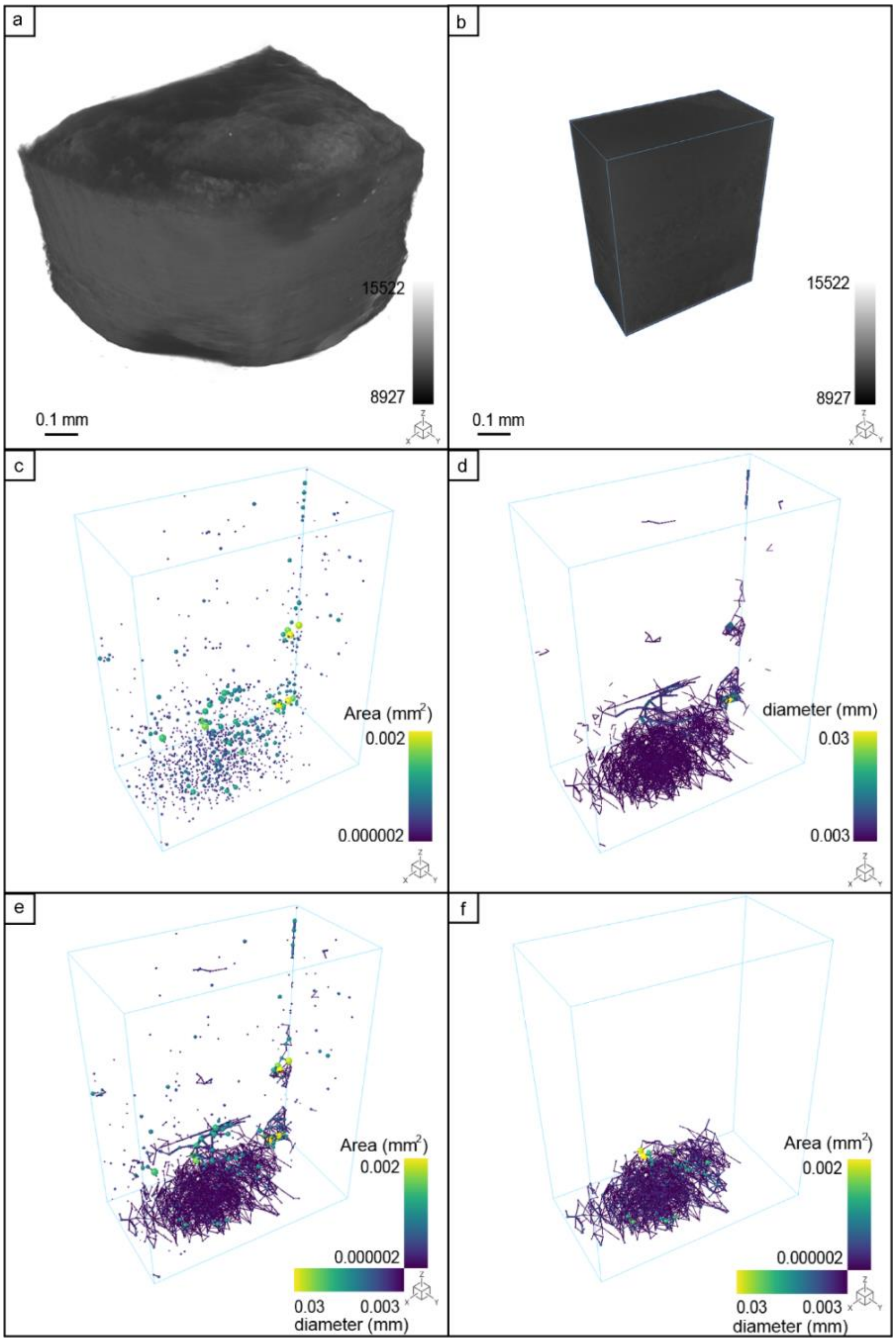

Figure 7. 3D Model analysis of the dolomitic shale-h sample using Micro-CT imagery: (a) High-resolution image obtained with a 10x objective lens and a pixel resolution of 0.72 µm; (b) Region of Interest (ROI) within the 3D model, measuring 0.52 x 0.50 x 1.00 mm^3; (c) Distribution of pore diameters ranging from 1.54 to 14.84 µm; (d) Throat diameters ranging from 0.003 to 0.03 mm; (e) Pore network connectivity, indicating a porosity of 3.51%; and (f) Effective porosity, estimated at 1.99%.

4.4 Rock Simulation

Rock simulations were performed using Dragonfly software to evaluate the diffusivity of the rocks under gas conditions (Table 4). The simulations provided insights into fluid transport behavior throughout the rock matrix, demonstrating that diffusivity variations represent trends associated with lamination-aligned pore distributions.

The seepage simulation results highlighted the significance of porosity evaluation and modeling for understanding fluid flow characteristics. Effective porosity tended to decrease along the direction during lamination, resulting in variations in fluid transport behavior. The diffusivity of calcareous shale was greatest along the z-axis of the parallel lamination (calcareous shale-h) at 0.022030 m^2/s, whereas the other axes demonstrated reduced diffusivity.

Conversely, for perpendicular laminations (calcareous shale-v), the diffusivity along the z-axis was lower at 0.00711 m^2/s, while the x-axis exhibited a higher diffusivity of 0.022030 m^2/s due to its alignment with the lamination direction. Dolomitic shale demonstrated the greatest diffusivity along the z-axis of the perpendicular lamination (dolomitic shale-v), recorded at 0.022080 m^2/s. In the parallel lamination (dolomitic shale-h), the z-axis diffusivity was significantly reduced at 0.001553 m^2/s, whereas the y-axis exhibited a higher diffusivity of 0.065590 m^2/s, consistent with the orientation relative to perpendicular lamination.

These simulations demonstrate that parallel laminations in calcareous shale improve pore connectivity, but dolomitic shale undergoes dissolution processes create wider and more continuous pore spaces, especially in perpendicular laminations. Porosity analyses indicated that calcareous shale contains high-porosity regions along parallel laminations, while dolomitic shale displays more isotropic porosity in perpendicular laminations relative to parallel layers. Understanding the diverse characteristics of micropore size distributions and their impact on fluid transport and diffusivity is crucial for enhancing predictions of fluid migration in gas shale reservoirs (Jing et al., 2021; Xu et al., 2022).

The microscale anisotropy and heterogeneity of rock formations strongly influence large-scale fluid migration pathways, which are especially important to the petroleum industry, where petrophysical properties are influenced by variations in rock composition, structural anisotropy, and depositional environments (Bollermann et al., 2022; He et al., 2014). A high density of porous structures generally correlates with increased diffusivity, improving the characterization of fluid movement paths (Bollermann et al., 2022).

Seepage simulations showed that calcareous shale demonstrated increased porosity and diffusivity along parallel laminations, while dolomitic shale exhibited superior porosity and diffusivity along perpendicular laminations. In calcareous shale, parallel laminations exhibited the highest diffusivity, while perpendicular laminations showed a reduction. In contrast, dolomitic shale demonstrated increased diffusivity along perpendicular laminations and decreased diffusivity along parallel laminations. The results highlight the correlation between lamination direction, porosity, and diffusivity, affirming that effective porosity and lamination orientation substantially affect fluid transport parameters. Macropore fluid transport dynamics can be further investigated through fluid injection techniques, which yield significant insights into permeability variations (Han et al., 2020)

Table 4 Diffusivity (m²/s) of rock simulations performed under air conditions, measured using the Dragonfly software.

Sample no./Axis	X-Axis	Y-Axis	Z-Axis
Calcareous shale-v	7.110000	0.002388	0.013650
Calcareous shale-h	0.006114	0.003627	0.022030
Dolomitic shale-v	0.000181	0.002306	0.022080
Dolomitic shale-h	0.006641	0.065590	0.001553

The distribution of anisotropic pore sizes varies across dimensions, with perpendicular laminations of calcareous shale-v showing pore sizes between 1.59 and 6.06 µm, while parallel laminations (calcareous shale-h) ranged from 1.21 to 8.28 µm. Pore diameters in dolomitic shale range from 0.77 to 10.75 µm for dolomitic shale-v and from 1.54 to 14.84 µm for dolomitic shale-h (Table 5). These characteristics directly affect fluid movement behavior among interconnected pores (Chumkratoke, 2016; Jing et al., 2021). However, the results demonstrate a more significant decrease in effective porosity for both perpendicular and parallel laminations. The effective porosity values for perpendicular and parallel laminations in calcareous shale were 0.83% and 1.75%, respectively. In dolomitic shale, porosity ranged from 3.27% for perpendicular laminations to 1.99% for parallel laminations (Table 5). The heterogeneous arrangement of micropores (<50 nm) significantly affects fluid transport and diffusivity (Chumkratoke, 2016; Jing et al., 2021; Xu et al., 2022). Cid et al. (2017) determined that the effective porosity of gas shale is typically lower than its total porosity.

The importance of these porosity trends is corroborated by seepage simulation results, which demonstrate that micropore fluid flow may be studied using advanced techniques such as fluid injection (Han et al., 2020). Understanding the diverse characteristics of micropore size distributions and their influence on fluid transport and diffusivity is crucial for enhancing predictions of fluid migration in gas shale reservoirs (Jing et al., 2021; Xu et al., 2022). The differences in pore and throat dimensions notably influence diffusivity in seepage simulations (Xu et al., 2022). The observed flattened pores indicate that pore shape is anisotropic and affected by rock deformation, resulting in seepage simulations that demonstrate anisotropic migration behavior (Bollermann et al., 2022).

This study confirmed a decrease in effective porosity in gas shales, showing a consistent decrease in total porosity that aligns with diffusivity trends observed in both perpendicular and parallel laminations. The decrease is linked to elevated diffusivity in pore distributions aligned with lamination orientations, which is essential for forecasting fluid transport behavior in these formations (Cid et al., 2017)

Table 5 Summary of porosity and diffusivity measurements for calcareous shale and dolomitic shale.

Sample no./Axis	Calcareous shale-v	Calcareous shale-h	Dolomitic shale-v	Dolomitic shale-h
Total SEM porosity (%)	5.54		3.04	
Pore diameter (μm)	1.59-6.06	1.21-8.28	0.77-10.75	1.54-14.84
Throat diameter (mm)	0.001-0.01	0.001-0.01	0.0002-0.002	0.003-0.03
Total 3D model porosity (%)	2.86	4.65	3.70	3.51
Effective 3D model porosity (%)	0.83	1.75	3.27	1.99
X-Axis diffusivity	High	Medium	Low	Medium
Y-Axis diffusivity	Low	Low	Medium	High
Z-Axis diffusivity	Medium	High	High	Low

5. Conclusions

The study examined the pore morphology, pore networks, and rock simulations of carbonate shale between calcareous shale and dolomitic shale from the Dat Fa Member of the Huai Hin Lat Formation. Scanning electron microscopy (SEM) imaging demonstrated that the pores in calcareous shale were primarily flat, parallel, and pinch-outs along the laminations, exhibiting a total porosity of 5.54%. The pore network model studies indicated that calcareous shale has a total porosity of 2.86% to 4.65%, with effective porosity values of 0.83% to 1.75% in the perpendicular and parallel orientations, respectively.

The SEM images of dolomitic shale exhibited laminations between dolomite and calcite, with a total porosity of 3.04% around mineral grains. The pore network model estimated total porosity values ranging from 3.51% to 3.70%, which declined to effective porosity values of 1.99% to 3.27% in the perpendicular and parallel orientations, respectively.

The pore network models demonstrated a heterogeneous pore distribution, characterized by a dense network of effective porosity that declines in particular areas. The observed trends in total and effective porosities, in combination with diffusivity across various dimensions of the rock, were associated with increased effective gas transport in particular lamination orientations. Seepage simulations revealed that calcareous shale displays increased diffusivity along parallel laminations, whereas dolomitic shale exhibits superior diffusivity along perpendicular laminations. Because the dolomitic shale is affected by the anisotropic distribution of pores, which results from the orientation of mineral grains in the rock. Although the porosity and permeability values are comparatively low, these attributes are essential for understanding the fluid migration pathways that directly affect the quality of tight reservoirs in unconventional petroleum systems. Furthermore, the findings indicate that these rocks possess potential utility as seals in the carbon capture and storage (CCS) sector.

6. Acknowledgments

We would like to express our sincere gratitude to the Dragonfly team at the Dragonfly Company, whose advanced imaging technologies and capabilities were crucial to the success of our study. We extend thanks to Dr. Zixiong Cao for his technical proficiency, guidance with sample analysis, and for providing access to the Dragonfly imaging tools for our research. We also express our profound appreciation to the Synchrotron facility at the Synchrotron Light Research Institute (SLRI), Ministry of Science and Technology, Thailand, for allowing access to advanced X-ray Tomography Microscopy (XTM) equipment. The high-resolution 3D imaging data obtained was essential to our analysis.

7. References

Arsairai, B., Chonglakmani, C., & Feng, Q. (2016a). Pore type characteristics of the Huai Hin Lat Formation in Sap Phlu Basin, northeastern Thailand: Contribution to the understanding of gas storage in fine-grained rocks. *Suranaree Journal of Science & Technology*, *23*(3). https://doi.org/https://api.semanticscholar.org/CorpusID:167215880

Arsairai, B., Feng, Q., Chonglakmani, C., & Glumglomjit, S. (2023). Source rock potential assessment of the Huai Hin Lat Formation, Sap Phlu Basin, Nakhon Ratchasima Province, northeastern Thailand. *Acta Geochimica*, *42*(1), 38-49.

Arsairai, B., Wannakomol, A., Feng, Q., & Chonglakmani, C. (2016b). Paleoproductivity and paleoredox condition of the Huai Hin Lat Formation in northeastern Thailand. *Journal of Earth Science*, *27*, 350-364. https://doi.org/https://doi.org/10.1007/s12583-016-0666-8

Askarova, A., Mukhametdinova, A., Markovic, S., Khayrullina, G., Afanasev, P., Popov, E., & Mukhina, E. (2023). An overview of geological CO_2 sequestration in oil and gas reservoirs. *Energies*, *16*(6), 2821. https://doi.org/https://doi.org/10.3390/en16062821

Bollermann, T., Yuan, T., Kulenkampff, J., Stumpf, T., & Fischer, C. (2022). Pore network and solute flux pattern analysis towards improved predictability of diffusive transport in argillaceous host rocks. *Chemical Geology*, *606*, 120997. https://doi.org/https://doi.org/10.1016/j.chemgeo.2022.120997

Chenrai, P., Assawincharoenkij, T., Jitmahantakul, S., & Chaiseanwang, P. (2022a). Geochemical characteristics of shale gas formation and the potential for carbon storage in Thailand: An example from the Triassic Huai Hin Lat Formation. *Frontiers in Earth Science*, *10*, 1085869. https://doi.org/https://doi.org/10.3389/feart.2022.1085869

Chitnarin, A., Kershaw, K., Promduang, A., & Tepnarong, P. (2022). Late triassic freshwater conchostracan, ostracods, and stromatolites from Huai Hin Lat Formation, northeastern Thailand. *Thai Geosci. J*, *3*(3), 32-50. https://doi.org/https://ph03.tci-thaijo.org/index.php/TGJ/article/view/1795

Chonglakmani, C., & Sattayarak, N. (1978). Stratigraphy of the Huai Hin Lat Formation (upper triassic) in northeastern Thailand. Regional conference on geology and mineral resources of Southeast Asia. 3,

Chumkratoke, C. (2016). *Modeling gas inflow for extremely low permeability shale using CFD*. Missouri University of Science and Technology. https://doi.org/https://www.proquest.com/dissertations-theses/modeling-gas-inflow-extremely-low-permeability/docview/1842606202/se-2

Cid, H., Carrasco-Núñez, G., & Manea, V. (2017). Improved method for effective rock microporosity estimation using X-ray microtomography. *Micron*, *97*, 11-21. https://doi.org/https://doi.org/10.1016/j.micron.2017.01.003

DMR. (2013). *Geologic map of Thailand*. Bangkok, Thailand, Department Of Mineral Resources.

Dyni, J. R. (2004). *Oil shale*. Elsevier. https://doi.org/https://doi.org/10.1016/B978-008044410-9/50007-3

Han, J., Han, S., Kang, D. H., Kim, Y., Lee, J., & Lee, Y. (2020). Application of digital rock physics using X-ray CT for study on alteration of macropore properties by CO_2 EOR in a carbonate oil reservoir. *Journal of Petroleum Science and Engineering*, *189*, 107009. https://doi.org/Application of digital rock physics using X-ray CT for study on alteration of macropore properties by CO_2 EOR in a carbonate oil reservoir

He, L., Zhao, L., Li, J., Ma, J., Lui, R., Wang, S., & Zhao, W. (2014). Complex relationship between porosity and permeability of carbonate reservoirs and its controlling factors: A case study of platform facies in Pre-Caspian Basin. *Petroleum Exploration and Development Online*, *41*(2), 225-234. https://doi.org/https://doi.org/10.1016/S1876-3804(14)60026-4

Javadpour, F., Fisher, D., & Unsworth, M. (2007). Nanoscale gas flow in shale gas sediments. *Journal of Canadian Petroleum Technology*, *46*(10). https://doi.org/https://doi.org/10.2118/07-10-06

Jing, D., Meng, X., Ge, S., Zhang, T., Ma, M., & Tong, L. (2021). Reconstruction and seepage simulation of a coal pore-fracture network based on CT technology. *PloS one*, *16*(6), e0252277. https://doi.org/https://doi.org/10.1371/journal.pone.0252277

Khan, D., Qiu, L., Liang, C., Mirza, K., Kashif, M., Yang, B., Kra, K. L., Wang, Y., & Li, X. (2022). Formation and distribution of different pore types in the lacustrine calcareous shale: insights from XRD, FE-SEM, and low-pressure nitrogen adsorption analyses. *ACS omega*, *7*(12), 10820-10839. https://doi.org/https://pubs.acs.org/doi/10.1021/acsomega.2c01001

Khositchaisri, W. (2012). *Petroleum geochemistry of Huai Hin Lat formation in Amphoe Nam Nao, Changwat Phetchabun and Amphoe Chumpae, Changwat Khon Kaen, Thailand* Chulalongkorn University].

Lin, W., Li, X., Yang, Z., Xiong, S., Luo, Y., & Zhao, X. (2020). Modeling of 3D rock porous media by combining X-ray CT and Markov chain Monte Carlo. *Journal of Energy Resources Technology*, *142*(1), 013001. https://doi.org/https://doi.org/10.1115/1.4045461

Lovatt Smith, P. F., Stokes, R. B., Bristow, C., & Carter, A. (1996). Mid-Cretaceous inversion in the northern Khorat Plateau of Lao PDR and Thailand. *Geological Society, London, Special Publications*, *106*(1), 233-247.

MacInnis, I. N., & Brantley, S. L. (1992). The role of dislocations and surface morphology in calcite dissolution. *Geochimica et Cosmochimica Acta*, *56*(3), 1113-1126. https://doi.org/https://doi.org/10.1016/0016-7037(92)90049-O

Meng, T., Liu, Z., Wu, F., Zhang, Z., Liang, X., He, Y., Wu, X., Yang, Y., & Gao, H. (2024). Coupled thermo-hydro-mechanical analysis of porous rocks: Candidate of surrounding rocks for deep geological repositories. *Journal of Rock Mechanics and Geotechnical Engineering*. https://doi.org/https://doi.org/10.1016/j.jrmge.2024.11.010

Rashid, F., Glover, P., Lorinczi, P., Collier, R., & Lawrence, J. (2015). Porosity and permeability of tight carbonate reservoir rocks in the north of Iraq. *Journal of Petroleum Science and Engineering*, *133*, 147-161. https://doi.org/https://doi.org/10.1016/j.petrol.2015.05.009

Saraf, S., & Bera, A. (2021). A review on pore-scale modeling and CT scan technique to characterize the trapped carbon dioxide in impermeable reservoir rocks during sequestration. *Renewable and Sustainable Energy Reviews*, *144*, 110986.

Song, R., Wang, Y., Sun, S., & Liu, J. (2021). Characterization and microfabrication of natural porous rocks: From micro-CT imaging and digital rock modelling to micro-3D-printed rock analogs. *Journal of Petroleum Science and Engineering*, *205*, 108827.

https://doi.org/https://doi.org/10.1016/j.petrol.2021.108827

Xu, K., Wei, W., Chen, Y., Tian, H., Xu, S., & Cai, J. (2022). A pore network approach to study throat size effect on the permeability of reconstructed porous media. *Water*, *14*(1), 77. https://doi.org/https://doi.org/10.3390/w14010077

Zhang, L., Shan, B., Zhao, Y., & Tang, H. (2018). Comprehensive seepage simulation of fluid flow in multi-scaled shale gas reservoirs. *Transport in Porous Media*, *121*, 263-288. https://doi.org/https://doi.org/10.1007/s11242-017-0958-1

Zhou, S., Yan, G., Xue, H., Guo, W., & Li, X. (2016). 2D and 3D nanopore characterization of gas shale in Longmaxi formation based on FIB-SEM. *Marine and Petroleum Geology*, *73*, 174-180. https://doi.org/https://doi.org/10.1016/j.marpetgeo.2016.02.033